



OPEN ACCESS

EDITED BY

Da-Hua Wei,
National Taipei University of Technology,
Taiwan

REVIEWED BY

Zhelong Jiang,
Stanford University, United States
Xiangjiu Guan,
Xi'an Jiaotong University, China

*CORRESPONDENCE

Seetha Mahalingam,
✉ seetha.phy@gmail.com
Chung-Li Dong,
✉ cldong@mail.tku.edu.tw

RECEIVED 03 April 2023

ACCEPTED 12 June 2023

PUBLISHED 22 June 2023

CITATION

Alageshwaramoorthy K, Mannu P,
Mahalingam S, Nga TTT, Chang H-W,
Masuda Y and Dong C-L (2023), Synthesis
and characterization of visible-light-
driven novel CuTa₂O₆ as a promising
practical photocatalyst.
Front. Chem. 11:1197961.
doi: 10.3389/fchem.2023.1197961

COPYRIGHT

© 2023 Alageshwaramoorthy, Mannu,
Mahalingam, Nga, Chang, Masuda and
Dong. This is an open-access article
distributed under the terms of the
[Creative Commons Attribution License
\(CC BY\)](https://creativecommons.org/licenses/by/4.0/). The use, distribution or
reproduction in other forums is
permitted, provided the original author(s)
and the copyright owner(s) are credited
and that the original publication in this
journal is cited, in accordance with
accepted academic practice. No use,
distribution or reproduction is permitted
which does not comply with these terms.

Synthesis and characterization of visible-light-driven novel CuTa₂O₆ as a promising practical photocatalyst

Krishnaprasanth Alageshwaramoorthy¹, Pandian Mannu²,
Seetha Mahalingam^{1*}, Ta Thi Thuy Nga², Han-Wei Chang^{3,4},
Yoshitake Masuda⁵ and Chung-Li Dong^{2*}

¹Department of Physics, Kongunadu Arts and Science College, Coimbatore, India, ²Research Center for X-ray Science and Department of Physics, Tamkang University, Tamsui, Taiwan, ³Department of Chemical Engineering, National United University, Miaoli, Taiwan, ⁴Pesticide Analysis Center, National United University, Miaoli, Taiwan, ⁵National Institute of Advanced Industrial Science and Technology (AIST), Nagoya, Japan

In this work, the novel CuTa₂O₆ phase was successfully synthesized by the hydrothermal and followed by the calcination process. The X-ray diffraction pattern confirms the formation of different phases. At a low temperature, CuTa₂O₆ exhibits the orthorhombic phase, whereas, at a higher temperature, it underwent a phase transition to a cubic crystal structure. X-ray photoelectron spectroscopic results suggest the presence of all the elements (Cu, Ta, and O). The optical studies were carried out using a UV-Vis DRS spectrophotometer. FESEM images confirm the spherical-shaped particles for the sample annealed at a high temperature. The local atomic and electronic structures around Cu and the contribution of the Cu oxidation state in the CuTa₂O₆ system were determined by X-ray absorption spectroscopy. To investigate the effective usage of CuTa₂O₆ in treating wastewater, its photocatalytic activity was investigated by evaluating its use in the photodegradation of MO dye under visible light irradiation. Moreover, the prepared CuTa₂O₆ photocatalyst exhibits significant photocatalytic activity in the degradation of MO dye and shows excellent stability; it is therefore a promising material for potential use in a practical photocatalyst. The CuTa₂O₆ photocatalyst suggests an alternative avenue of research into effective photo-catalysts for solar hydrogen water splitting.

KEYWORDS

phase transition, photocatalytic activity, dye degradation, X-ray absorption spectroscopy (XAS), visible light irradiation

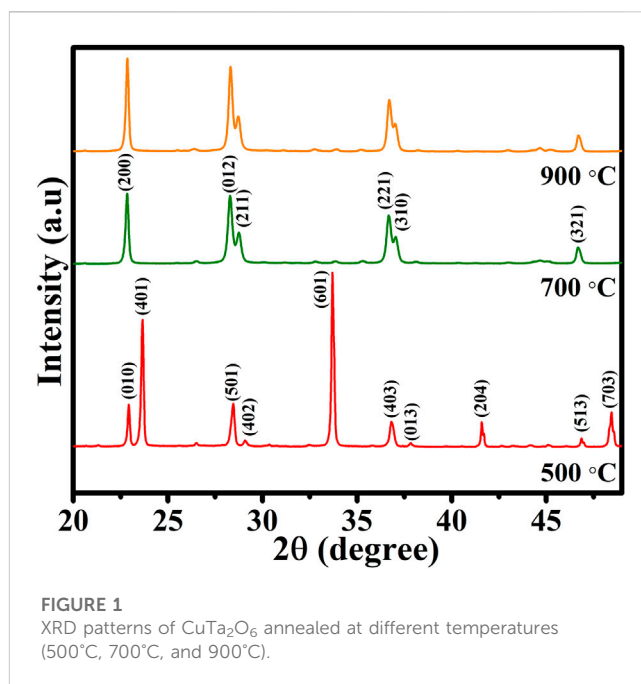
1 Introduction

Rapid population and industrial growth have made the environment a serious problem globally. Clean water is important for global and economic development, and the agricultural, industrial, and domestic sectors require huge quantities of unpolluted water. Over the last few decades, polluted water has caused major problems, especially for aquatic organisms, animal ecosystems, and humans (Gheytanzadeh et al., 2022). Notably, the dyes from textile, leather, fabric, paper, cosmetics, pulp, food, dye synthesis, plastics, and pharmaceuticals generate wastewater that emerges as threatening pollutants to the environment (Oyewo et al., 2022). Just a few layers of dye on the surface of the water

blocks sunlight and disturb the photosynthesis of aquatic species below (Abdelrahman et al., 2019). Primary techniques such as coagulation, filtration, reverse osmosis, and flocculation can be used to remove dye from wastewater. Instead of degrading the pollutants; these techniques simply convert the pollutants from one form to another, causing secondary pollution (Ajmal et al., 2014). Therefore, many methods have been employed for wastewater treatment such as chlorination, flocculation, ozonation, adsorption, photocatalysis, chemical oxidation, and biodegradation (Hodges et al., 2018; Yang et al., 2020; Sahoo et al., 2022). Among, advanced oxidation processes (AOPs) such as H_2O_2/UV processes, and photodegradation are commonly used for clean energy and biodegradable catalysts for the removal of pollutants. Additionally, the photocatalyst includes the whole mineralization of organic pollutants into carbon dioxide and water without any harmful by-products is being as the most promising technique (Yang et al., 2020) (Sahoo et al., 2022).

Heterogeneous photocatalysis using semiconductors is a broad field that involves dye photodegradation from wastewater (Majhi et al., 2021; Louis et al., 2022). TiO_2 is a well-known photocatalyst whose crystalline structure can be modified to increase its photocatalytic activity in water treatment. However, the large bandgap of anatase TiO_2 (3.2 eV) limits its efficiency under solar light: it uses only 4% of the total solar spectrum (Rose et al., 2022). Therefore, a more efficient, chemically stable photocatalyst that is active in the visible light region must be developed. Various semiconductors like ZnO, Bi_2O_3 , and SnO_2 , as well as also metal-chalcogenides like Cds, CdSe, CdTe, and Pbs have been investigated for this purpose (Djurišić et al., 2014; Ramchiary, 2020; Li et al., 2023). Several strategies have been used to improve their photocatalytic activity, doping or coupling of low bandgap semiconductors with suitable materials can effectively improve photocatalytic activity under visible light (Zhang et al., 2006; Zhou et al., 2009; Xu et al., 2012a). It is well known that copper-based metal oxides are p-type semiconductors, commonly used in solar energy applications owing to their narrow band gap of ~ 1.2 eV. Compared to other regularly used p-type materials like NiO, it exhibits higher charge carrier motilities ($100\text{ cm}^2\text{v}^{-1}\text{s}^{-1}$) while NiO has ($0.53\text{ cm}^2\text{v}^{-1}\text{s}^{-1}$). They are more stable in aqueous media than Group III-V or II-VI semiconductors (Sullivan et al., 2016). The narrow band gap and good stability of copper make it suitable for photocatalytic applications (Sibhatu et al., 2022).

On the other hand, great interest has been shown in the photocatalytic activity of Tantalum-based materials that include Ta_2O_5 , TaON, and Ta_3N_5 (Zhang et al., 2014; Suzuki et al., 2017; Gomes et al., 2018). Apart from these materials, transition metal tantalates and antimonates (general formula $M'M''_2O_6$, where: $M' = Cu/Zn$, and $M'' = Ta/Sb$) emerging in various research due to their excellent magnetic, electrical, optical, thermoluminescence and more importantly the catalytic properties (Nguyen et al., 1996; Kato et al., 2002; Dutta et al., 2013; Noto et al., 2013). These composites represent an important group of semiconductors, characterized by high thermal stability (above $1,000^\circ\text{C}$) and ease of modification of their physicochemical properties. Therefore, among these materials, $CuTa_2O_6$ has been a promising candidate in fundamental research and numerous applications (Nguyen et al., 1996; Kato et al., 2002; Dutta et al., 2013; Noto et al., 2013). Available literature suggests that the $CuTa_2O_6$ compound is formed in the binary system of $CuO-Ta_2O_5$



oxides (Golubev et al., 2017). Moreover, $CuTa_2O_6$ also occurs in two polymorphic varieties which include monoclinic and tetragonal (Krabbes and Langbein, 1996). Some authors reported that there is an orthorhombic variety of this $CuTa_2O_6$ compound as well (Vincent et al., 1978). Even though many studies have been carried out on $CuTa_2O_6$ that include high dielectrics, exceptional photoelectric performance, and chemical stability, there are only limited investigations done on the photocatalytic properties of $CuTa_2O_6$.

This work demonstrates the fundamental parameters involved in the photocatalytic activity of copper tantalite, which can be used as a water-splitting material due to its promising properties. To the best of the authors' knowledge, photodegradation of MO dye under visible light irradiation on the $CuTa_2O_6$ phase has not been previously investigated. Thus, a novel $CuTa_2O_6$ -based photocatalyst is prepared by a hydrothermal and calcination process, and its photocatalytic performance under visible light irradiation is studied.

2 Materials and methods

All of the chemical reagents including copper nitrate trihydrate ($Cu(NO_3)_2 \cdot 3H_2O$) and tantalum chloride ($TaCl_5$), were purchased from Sigma Aldrich (United States) and used without further purification. De-ionized water was used as a solvent throughout the experiment and ethanol was used to wash the prepared photocatalyst. Methyl orange (MO) dye was purchased from Merck and used as a model pollutant.

In a typical synthesis procedure, an equal amount (0.1M) of tantalum chloride and copper nitrate trihydrate was dissolved in 30 mL of de-ionized water, which was then stirred continuously at room temperature to yield a homogeneous solution. Then, this solution was transferred to a 50 mL Teflon-lined beaker and kept in a stainless-steel autoclave at 180°C for 8 h. After attaining room temperature, the obtained product was washed several times with

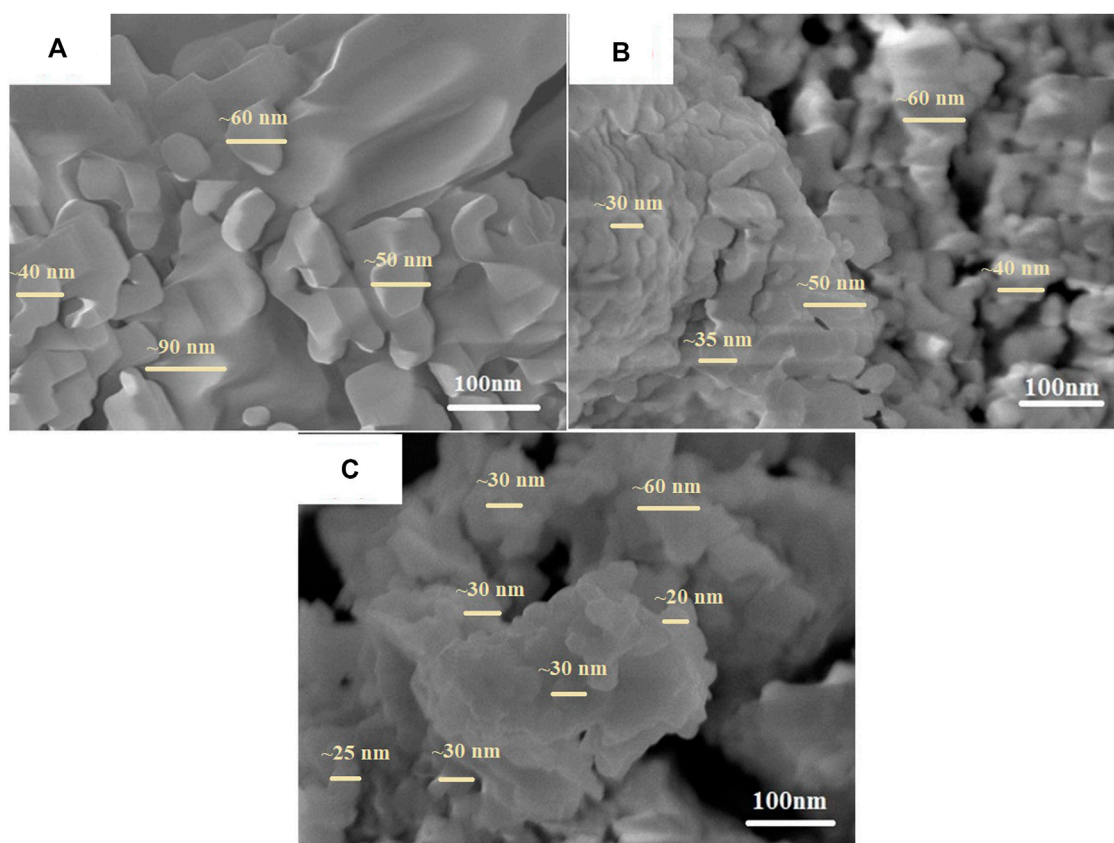


FIGURE 2
FESEM images of CuTa_2O_6 samples annealed at (A) 500°C, (B) 700°C, and (C) 900°C.

de-ionized water and ethanol followed by drying at 80°C for an hour. The dried powder was collected and annealed at 500°C, 700°C, and 900°C.

2.1 Characterization

The crystal structure and the phase purity of the prepared samples were confirmed by X-ray diffraction (Shimadzu 6,000) with Cu-K α radiation, $\lambda = 1.5406 \text{ \AA}$. The surface morphology was analyzed using a field emission scanning electron microscope (FESEM model—CARLZEISS SIGMA HV). The chemical composition analysis was studied by Thermo Scientific K-Alpha X-ray Photoelectron Spectroscopy (using ESCA-3400 XPS from Kratos Analytical, Shimadzu). The optical band gap was estimated from UV-Vis diffused reflectance spectra using the JASCO V-670 double-beam spectrophotometer model. Synchrotron X-ray absorption spectra (Cu K-edge), including X-ray absorption near edge structure (XANES) and extended X-ray absorption fine structure (EXAFS) spectra, were obtained at BL17C of the National Synchrotron Radiation Research Center (NSRRC), Taiwan. The specific surface area was calculated from N_2 adsorption-desorption isotherms measured using the ANTON PAAR NOVATOUGH LX2 (Graz, Austria), using the Brunauer–Emmett–Teller (BET) equation.

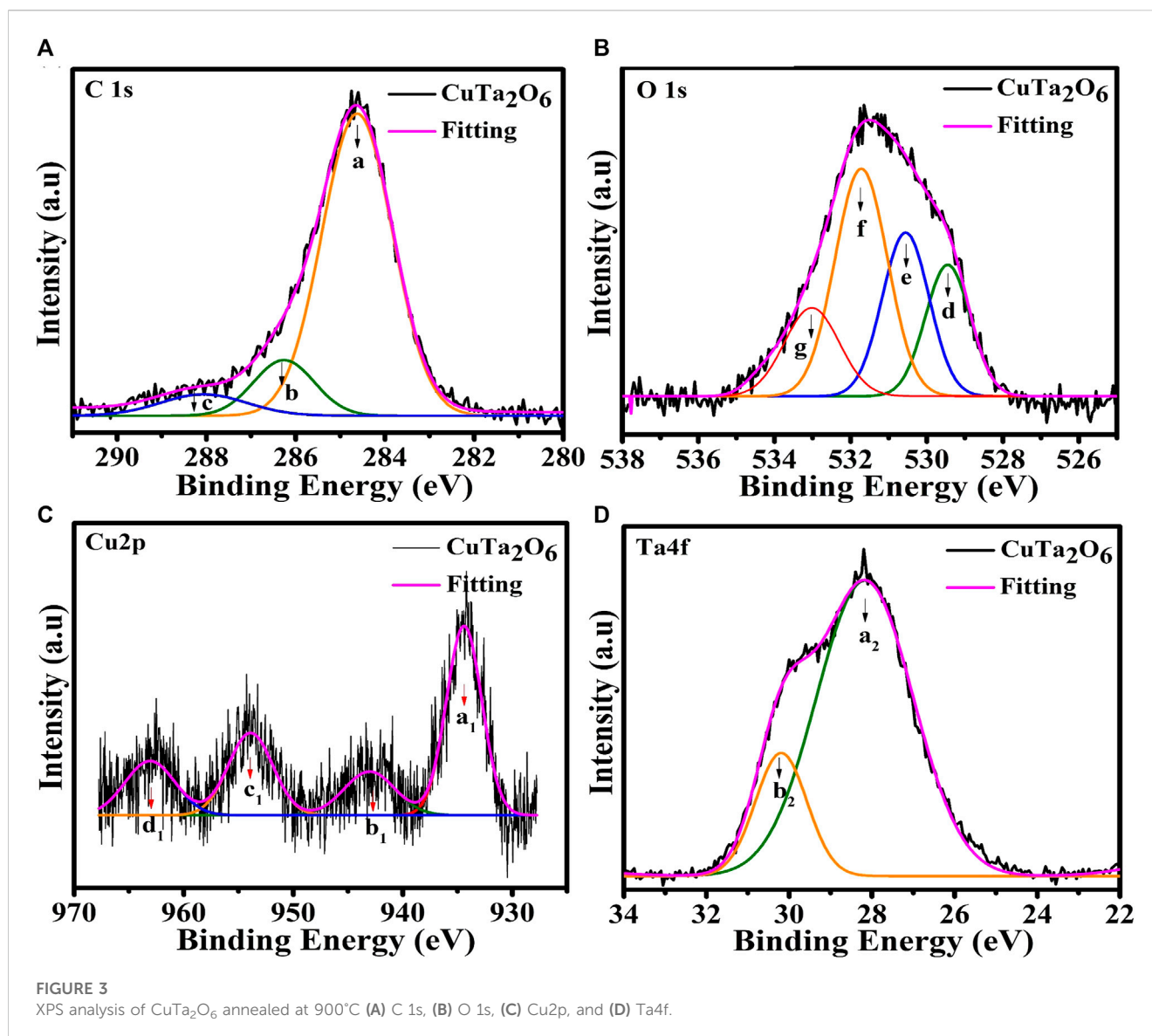
2.2 Photocatalytic experiment

The photodegradation of MO dye was examined in the presence of the prepared CuTa_2O_6 photocatalyst. In a typical experiment, 50 mg of the photocatalyst was added to 100 mL of aqueous MO with an initial concentration of 10 mg/L. Before irradiation, the mixture was continuously stirred at room temperature in the dark for 30 min to achieve an adsorption/desorption equilibrium. Then, the mixed solution was irradiated with visible light using a 75 W high-pressure mercury vapor lamp. During the irradiation, about 2 mL of the suspension was taken at regular intervals (10 min) and analyzed using the UV-Vis spectrophotometer to determine the concentration of MO dye; the characteristic absorption of MO was about 464 nm (Mageshwari et al., 2013).

3 Results and discussion

3.1 Structural analysis

Figure 1 shows XRD patterns of the prepared CuTa_2O_6 at different annealing temperatures. The diffraction peak reveals the polycrystalline nature of the prepared CuTa_2O_6 phase. The sample annealed at 500°C exhibits the orthorhombic phase of CuTa_2O_6 and agrees with JCPDS card no: 87–0,357. Then, increasing the annealing temperature to 700°C



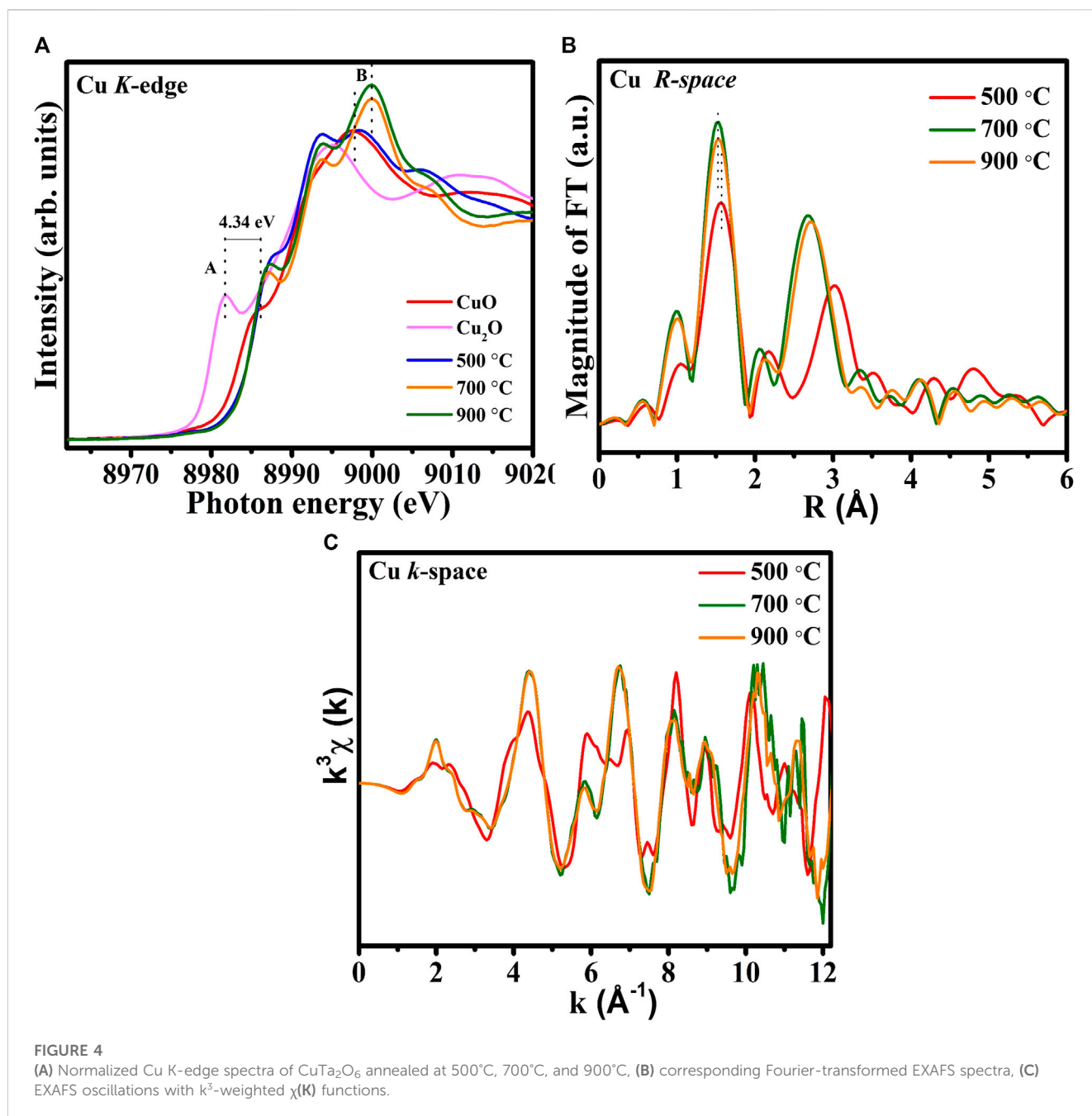
led to the formation of a different phase. The observed diffraction peaks are associated with the cubic phase of CuTa_2O_6 , which agrees with JCPDS card 70-0,611. Further increase in the annealing temperature to 900°C did not modify the phase formation. Therefore, increasing the annealing temperature significantly affects the phase formation of CuTa_2O_6 . The intensity of the diffraction peaks is higher, and the full width at half maximum (FWHM) is also slightly increased with an increase in the annealing temperature. The average crystallite size was calculated using the Debye-Scherrer formula $D = \frac{K\lambda}{\beta \cos \theta}$ where K is the shape factor of the particles that are commonly called the Scherrer constant ($k = 0.89$); λ is the wavelength of the X-ray radiation ($\lambda = 0.1542 \text{ nm}$ Cu-K α radiation); θ is the Bragg angle, and β is the FWHM of the peak.

The difference in the XRD peak width is small between 700°C and 900°C . However, the actual variation is shown in [Supplementary Figure S1](#) (supporting information), which evidences the increased value for full width at half maximum (FWHM). The intensity of the diffraction peaks and the FWHM also increased as the temperature increased. The higher the FWHM, the smaller the crystallite according to the Debye-Scherrer

formula. Therefore, the calculated average crystallite size is found to be 32.28 nm, 29.79 nm, and 28.13 nm for the samples that were annealed at 500°C , 700°C , and 900°C respectively. An increase in the annealing temperature reduces the crystallite size, this could be due to the higher annealing temperature which might produce a relatively large temperature gradient within the submicrospheres, resulting in the formation of solid/liquid biphasic core-shell structures through the non-equilibrium heating process (Tao et al., 2013). As heterogeneous nucleation only needs a low activation energy, the co-existence of heterogeneous phases can be helpful for the crystalline nucleation of CuTa_2O_6 . Also, it is believed that the more generated nuclei, the smaller the crystallite size.

3.2 Morphological studies

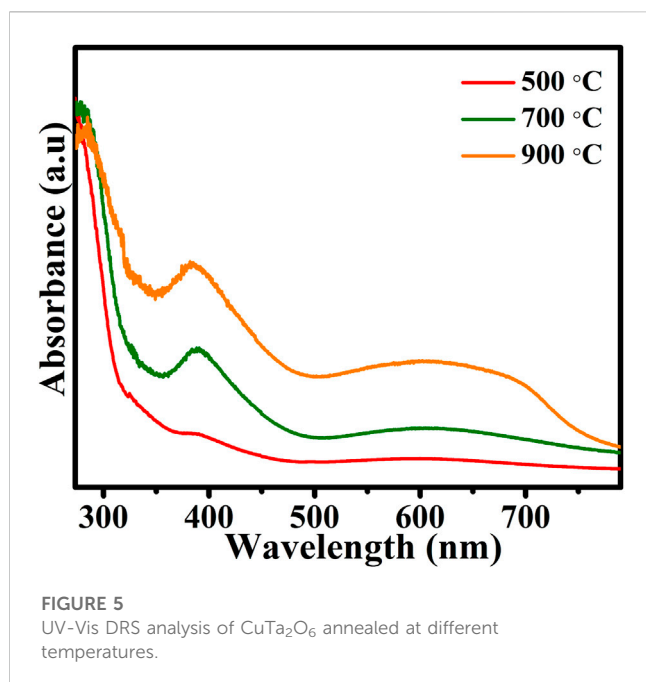
Figure 2A displays the nearly spherical shaped structure and uniform in size for the sample annealed at 500°C . It seems an increase in the annealing temperature to 700°C lead to



agglomeration of these particles, as shown in Figure 2B. Further increase in the annealing temperature (900°C) produces more agglomerated spherical-shaped particles with irregular distribution throughout the surface. As a result of the higher temperature, irregular particle shapes are fused via adhesion.

Similar to the estimated average crystallite size from the XRD results, the particle is also assumed to be smaller in the sample annealed at 900°C as the particles may be composed of an agglomeration of many crystallites (as marked in Figure 2), which results in the formation of irregular and deformed particle shapes at higher annealing temperatures. Consequently, the smaller the crystallite size, the smaller the

particle size. From Figures 2A–C, it seems the grains are dissimilar in different regions. Therefore, the particle size is likely to be different among the samples annealed at 500°C, 700°C, and 900°C as pointed out in Figure 2. For more evidence, the estimated average grain size is about 70 nm for a 500°C annealed sample. Then, it seems the average grain size gets reduced to ~40 nm at 900°C and is smaller than the sample annealed at 700°C (~50 nm). This implies that these particles/grains observed in the SEM image are composed of many crystallites/grains. Further, it is believed that the SEM image of the sample annealed at 900°C has composed of small size particles/grains than the other annealed samples.



3.3 X-ray photoelectron spectroscopy analysis

The elemental composition and valence state of the prepared samples were determined by the XPS technique. Figure 3 shows the recorded XPS data of the sample that was annealed at 900°C. The peak features a, b, and c are deconvoluted from the recorded C 1s spectra as shown in Figure 3A. The characteristic feature at 284.6 eV is sp²-hybridized carbon (C-C) that was adsorbed on the surface of the prepared sample (Khalid et al., 2013). Additionally, peaks at 286.2 eV, and 288.1 eV are related to the hydroxyl carbon (C-O), and carboxyl carbon (O=C-O), respectively (Liang et al., 2017). The measured O 1s spectra were deconvoluted into three peaks (Features d, e, and f), as shown in Figure 3B. The presence of various oxygen ions in CuTa₂O₆ with potentially different coordination environments (more Cu-coordinated or more Ta-coordinated), accounts for the deconvolution of the O 1s signals into multiple components. A peak at 529.6 eV (feature d) could be related to the CuO lattice oxygen peak as the binding energy of the lattice oxygen for the bulk samples was frequently found to be slightly higher than that for the nanostructures (Svintsitskiy et al., 2013). Furthermore, the peaks at 530.6 eV and 531.7 eV (features e and f) are associated with Ta-O and Ta=O, respectively. This main peak (feature f) could be attributed to the bulk oxygen ions affected by charge imbalance due to the presence of oxygen vacancy. An additional shoulder peak at 533.0 eV (feature g) is attributed to an oxygen species that is coupled to hydroxyl or hydrated molecules. Consequently, the prepared CuTa₂O₆ phases may contain O-H groups (Chennakesavulu and Ramajaneya Reddy, 2015). The high-resolution pattern of Cu 2p as displayed in Figure 3C exhibits the characteristic peaks at 934.2 eV (a₁ feature) and 954.1 eV (c₁ feature) that correspond to Cu 2p_{3/2} and Cu 2p_{1/2}, respectively, confirming the presence of Cu²⁺. The two other peaks at 943.1 eV (b₁ feature) and 962.3 eV (d₁ feature) are identified as shake-up satellite

peaks of Cu 2p_{3/2} and Cu 2p_{1/2} respectively. The shake-up peaks may have arisen from an unfilled Cu 3d⁹ shell, suggesting the presence of Cu₂O and Cu²⁺ in the prepared sample (Chennakesavulu and Ramajaneya Reddy, 2015) (Muthu Gnana Theresa Nathana et al., 2018). Figure 3D shows two peaks of Ta 4f_{7/2} (a₂ feature) and Ta 4f_{5/2} (b₂ feature) at 28.2 eV and 29.5 eV indicate the presence of tantalum in the Ta⁵⁺ oxidation state (Wang et al., 2012).

3.4 X-ray absorption spectroscopy (XAS) analysis

Figure 4A compares the Cu K-edge XANES spectra of the 500°C-, 700°C-, and 900°C-annealed CuTa₂O₆ phase with those of CuO (+1 oxidation state) and Cu₂O (+2 oxidation state) references. The rising-edge peak at ~8,980 eV for Cu₂O reveals the oxidation state of Cu¹⁺ (Kau et al., 1987). The absence of a pre-edge peak appears in the Cu K-edge XANES spectra is consistent with previous reports (Bera et al., 2002) (Khemthong et al., 2013). The main absorption peak around ~9,000 eV reveals the 1s-4p transition, which merges into the continuum states (Khemthong et al., 2013). A shoulder peak (feature A) in the energy range 8,985–8,990 eV is attributed to the 1s → 4p_z transition (shakedown). The energy shift of this feature (feature A) from Cu₂O to CuO is about 4.34 eV suggesting the valence state change from Cu¹⁺ to Cu²⁺. The Cu K-edge spectra of CuTa₂O₆ have two regions that include a shoulder peak and a main absorption peak (feature A and feature B). It seems the peak feature (feature A) of all the annealed CuTa₂O₆ is close to that of CuO, revealing the oxidation state of Cu²⁺ (Kau et al., 1987) (Lim et al., 2019). Then, the main absorption peak (feature B) of annealed at 500°C is also similar to those CuO reference samples again confirming the oxidation state of Cu²⁺. However, the main absorption peak (feature B) of annealed 900°C shows a higher intensity compared to the annealed 700°C suggesting the existence of more oxidation state of Cu²⁺. Also, this main absorption peak of located at a higher energy than the sample that was annealed at 500°C (feature B) so it is believed to have a more oxidation state.

To determine variations in the local atomic environment around Cu in the CuTa₂O₆ catalysts, the Fourier-transformed k³-weighted Cu K-edge spectra were obtained, as shown in Figure 4B. From the 500°C-annealed CuTa₂O₆, the major peaks at 1.56 Å and 3.01 Å correspond to Cu-O and Cu-Cu bonds, respectively (Nasir et al., 2017). The slight contraction in Cu-O bond length and the shortening in Cu-Cu/Ta bond at >900°C indicates the presence of more oxygen vacancies and cationic vacancies. Commonly, the contracted bond lengths are associated with an increase in the oxidation state. Therefore, the slight contraction in the Cu-O bond at 900°C compared to the 500°C, is also accompanied by the increased oxidation state of Cu. This contraction in the Cu-O bond also suggests the higher coordination number in Cu-O first shell. It is believed that this contraction in Cu-O bond length could be due to the strong interfacial interaction among the Cu-O-Ta materials. It is assumed that the oxidation state of Ta is also to be different in these samples. Particularly, an increase in annealing temperature might lead to an alteration in the valence state of the absorbing atoms in the sample annealed at 900°C. This considerable variation in the coordination of Cu-O and Cu-Cu/Ta suggests the phase transformation of CuTa₂O₆, as

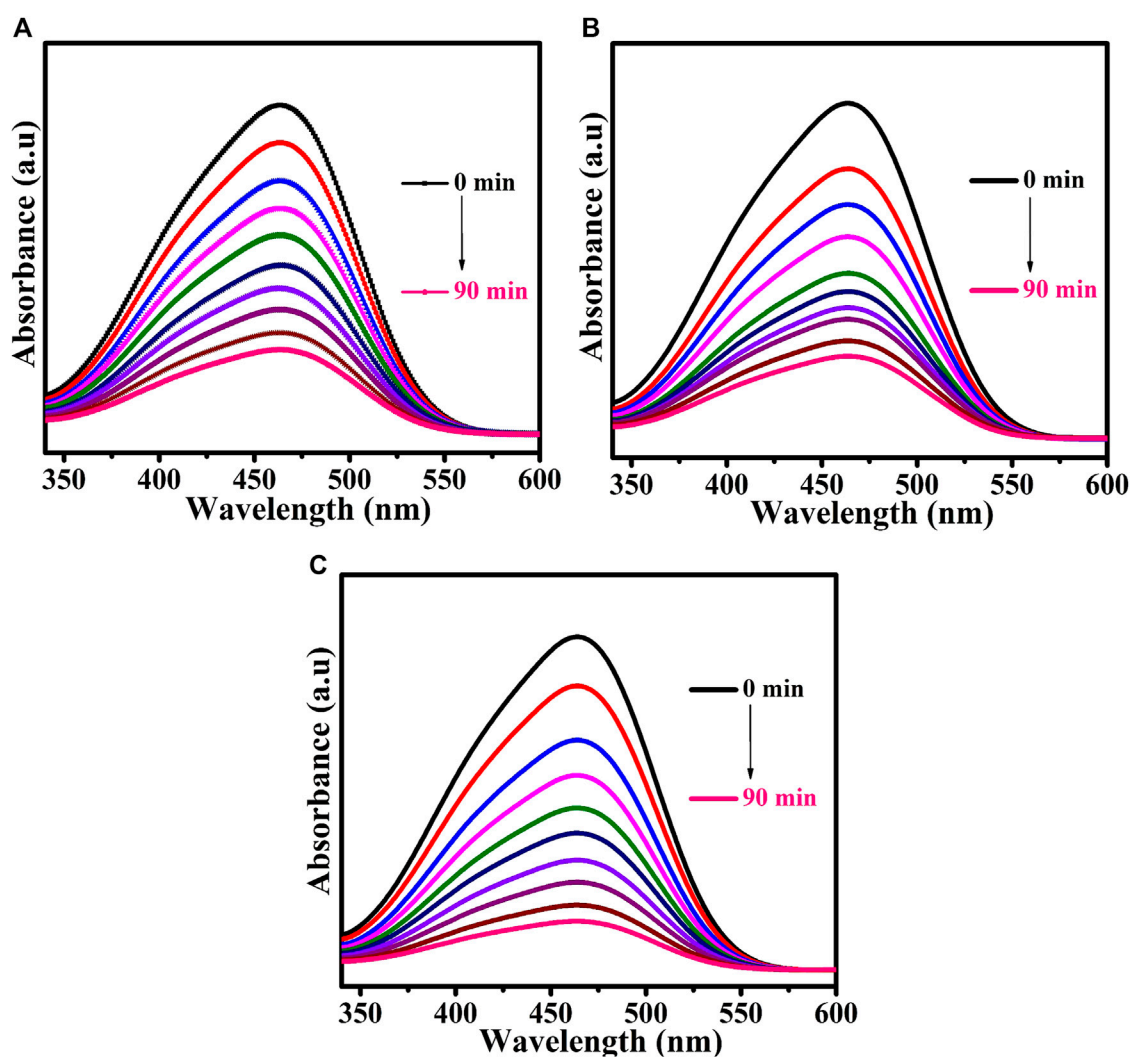


FIGURE 6
Time-dependent UV-Vis absorption spectra of MO dye solution without the addition of H_2O_2 for samples annealed at (A) 500°C, (B) 700°C, and (C) 900°C.

evident from the structural analysis. The FT-EXAFS oscillations of the CuTa_2O_6 catalysts exhibit different profiles specifically for sample annealed at 500°C, suggesting dissimilar coordination environments of the Cu-O sites as presented in CuTa_2O_6 in Figure 4C.

3.5 Optical studies

The UV-Vis DRS of the prepared CuTa_2O_6 phase was analyzed and is shown in Figure 5. All the prepared samples present a broad absorption range in the visible light region. The redshift that was observed with an increase in annealing temperature suggests that annealing increases sensitivity to visible light. The bandgap energy (E_g) of each prepared catalyst was estimated using the relation $E_g = 1,240/\lambda_g$ (eV), where λ_g is the absorption edge, which was obtained from the intercept between the tangent of the absorption curve and the abscissa. The estimated band gap energy of the samples that were

annealed at 500°C, 700°C, and 900°C corresponds to 3.85 eV, 3.66 eV, and 3.26 eV, respectively. A decrease in the bandgap energy is observed for the sample annealed at a higher temperature (900°C). This could be attributed to the transition of the band from Cu 3d⁺ O 2p orbital to Ta 5d orbital as Cu 3d¹⁰ state may contribute to the valence band of the semiconductor, as similar behavior also reported on the materials such as metal oxides and sulfide photocatalysts (Xu et al., 2012b).

3.6 Photocatalytic activity

Methyl orange dye was used as a model pollutant. The UV-Vis DRS analysis demonstrated that the prepared CuTa_2O_6 phase was active in the visible region. The photocatalytic process was carried out under visible light irradiation. Figure 6 shows the time-dependent UV-Vis absorption spectra of MO dye solution without and with the addition of H_2O_2 for the samples annealed at different temperatures (a) 500°C, (b) 700°C, and (c) 900°C. The

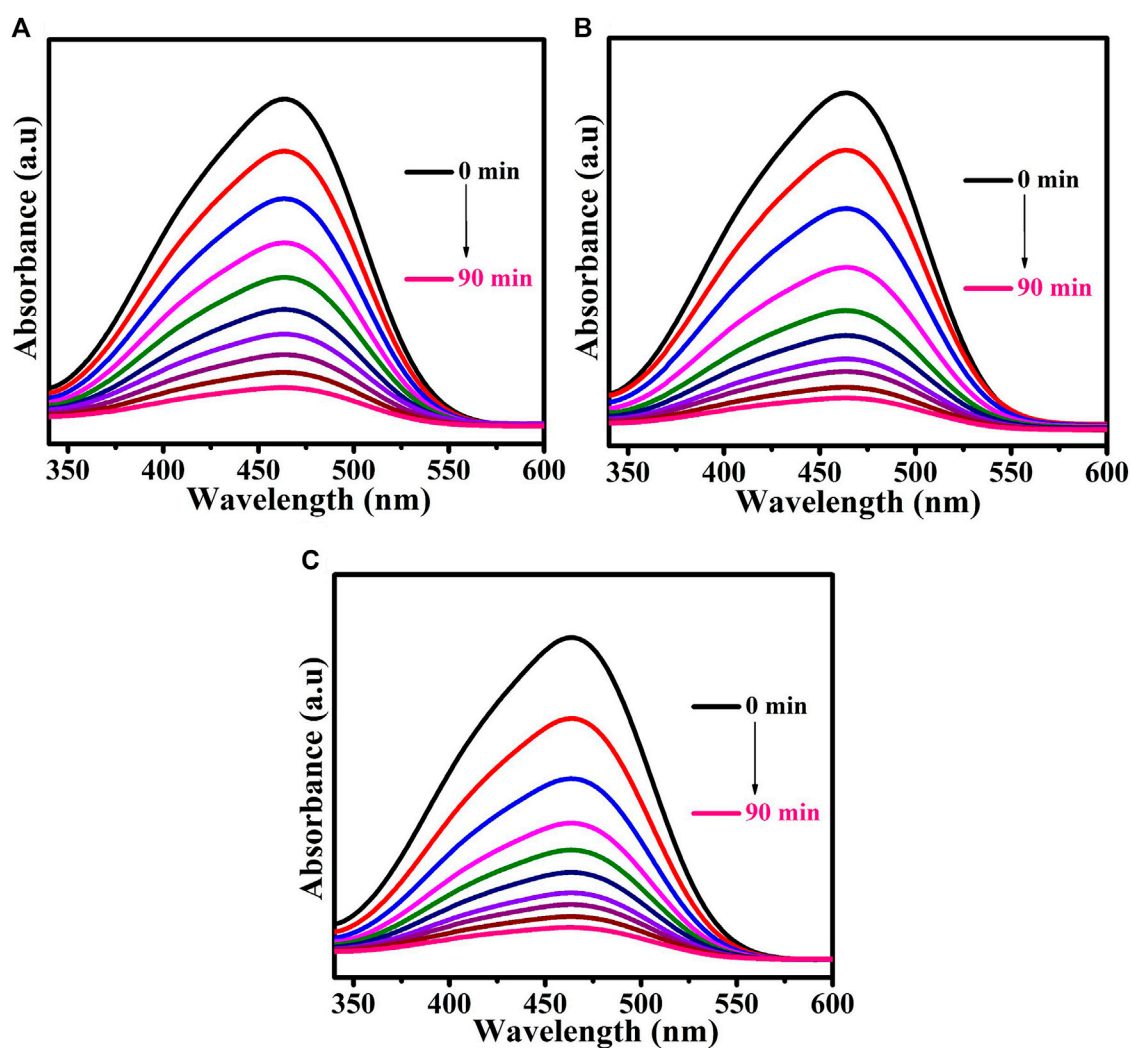


FIGURE 7
Time-dependent UV-Vis absorption spectra of MO dye solution for samples annealed at (A) 500°C, (B) 700°C, and (C) 900°C following the addition of H₂O₂.

UV-Vis DRS spectra of the MO dye solution show a characteristic peak at 464 nm. From Figure 6; Figure 7, the intensity of this characteristic peak gets decreases as the duration of exposure to light increases. At 90 min of exposure, the intensity of the peak was significantly reduced in comparison with 0 min, and the aqueous solution was colorless, indicating the decomposition of the dye molecules. The continuous disappearance of the absorption band suggests that the functional group of the MO dye is broken down (Xu et al., 2012b).

Figure 8A displays the estimated degradation efficiency of MO dye in the absence of H₂O₂. The percentage degradation efficiency was calculated as,

$$\text{Degradation (\%)} = \frac{C_0 - C}{C_0} \times 100\%$$

where C₀ is the initial concentration of MO dye and C is the concentration of the dye following irradiation for time t. The graph in Figure 8A displays the degradation efficiencies of the

samples annealed at 500°C, 700°C, and 900°C were found to 70.4%, 74.37%, and 81.3%, respectively. The sample annealed at 900°C shows the highest degradation efficiency revealing its superior photocatalytic activity. The increase in photodegradation efficiency can be attributed to a decrease in crystallite size, as agrees with the XRD results. Crystallite shrinkage increases the surface area-to-volume ratio of the catalyst, increasing the number of reactive sites and surface hydroxyl groups (Li et al., 2011). A large surface-area-to-volume ratio favors the reaction/interaction between the photocatalyst and the dye molecules, resulting in higher degradation efficiency. XRD results evidences that the samples annealed at 700°C and 900°C have similar phase structures and crystallinities. However, the sample annealed at 900°C exhibit a better photocatalytic performance whoci could be due to the existence of smaller crystallite size and more surface defects in materials. Smaller crystallite size corresponds to a larger total number of atoms with unsaturated coordinates on the surface, and these atoms have significantly improved photocatalytic

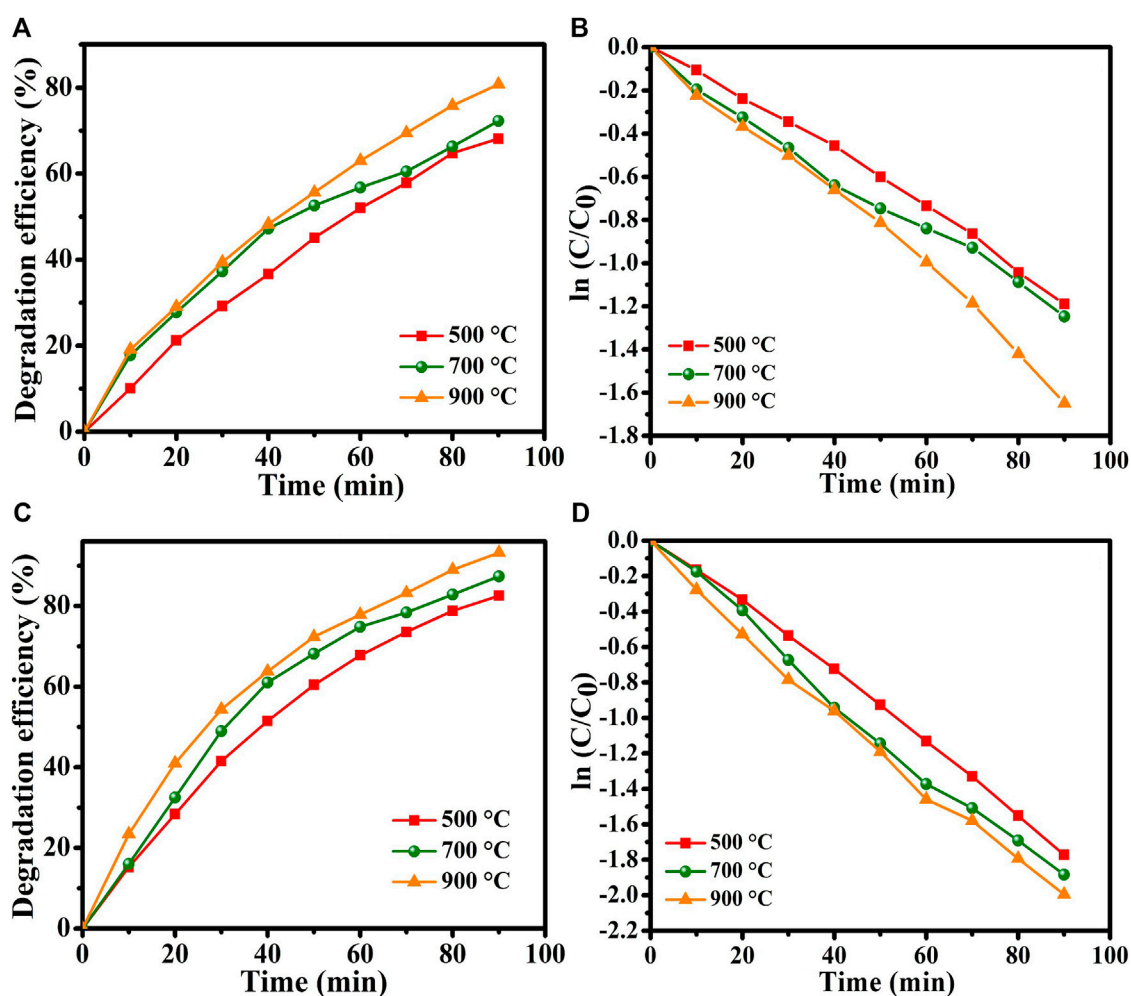


FIGURE 8

(A) Degradation efficiency of MO dye without H_2O_2 , (B) photodegradation rate. (C) Degradation efficiency of MO dye with H_2O_2 , (D) photodegradation rate.

activity. Additionally, the recombination of electrons and holes decreases as the crystallite size reduces, and thus the generated electrons and holes are transferred readily to the surface of the catalyst, favoring the process (Mageshwari et al., 2013).

To examine the surface area and porous structure of the prepared $CuTa_2O_6$ samples, BET surface analysis was carried out using nitrogen isothermal adsorption-desorption. Supplementary Figures S2A–C displays the isotherm curves of $CuTa_2O_6$ at different annealed temperatures along with the estimated pore-size distribution using the BJH method (Supplementary Figures S2D–F). The calculated specific surface area and BJH desorption Pore volume are presented in Supplementary Table S1. Generally, the surface area to volume ratio of nanomaterial plays a substantial role in influencing the material's properties (Xia et al., 2012). When the particle size decreases, there is an enhancement in the surface area-to-volume ratio (Liu et al., 2015). Consequently, the sample annealed at 900 °C shows a higher BET surface area ($10.96 \text{ m}^2/\text{g}$) than the other samples ($9.07 \text{ m}^2/\text{g}$ for 500 °C and $7.56 \text{ m}^2/\text{g}$ for 700 °C), indicating a greater number of existing active sites. We, therefore, believe that the large specific surface area benefits better

access and diffusion of liquid and gaseous reactants, which is beneficial for photocatalytic reactivity. The increased pore size distribution in the BJH desorption process is also likely to improve the photocatalytic performance of the materials (Supplementary Figures S2D–F).

The kinetics of the process importantly affect the rate at which pollution is removed. The kinetics of photocatalysis were determined from experimental data using the Langmuir–Hinshelwood model.

$$\ln \frac{C_0}{C} = K_r t$$

Here, K_r is the degradation rate constant and t is the degradation time. The degradation rate constant K_r is calculated from the slope of the kinetic plot of the natural logarithm of the concentration ratio $\ln(C/C_0)$ versus the irradiation time t in minutes. Figure 8B plots this curve for MO dye in the absence of H_2O_2 . The concentration ratio varies linearly with time suggest that the photodegradation of MO dye follows first-order kinetics. The degradation rate constants $K_r t$ for the samples that were annealed at 500 °C, 700 °C, and 900 °C are

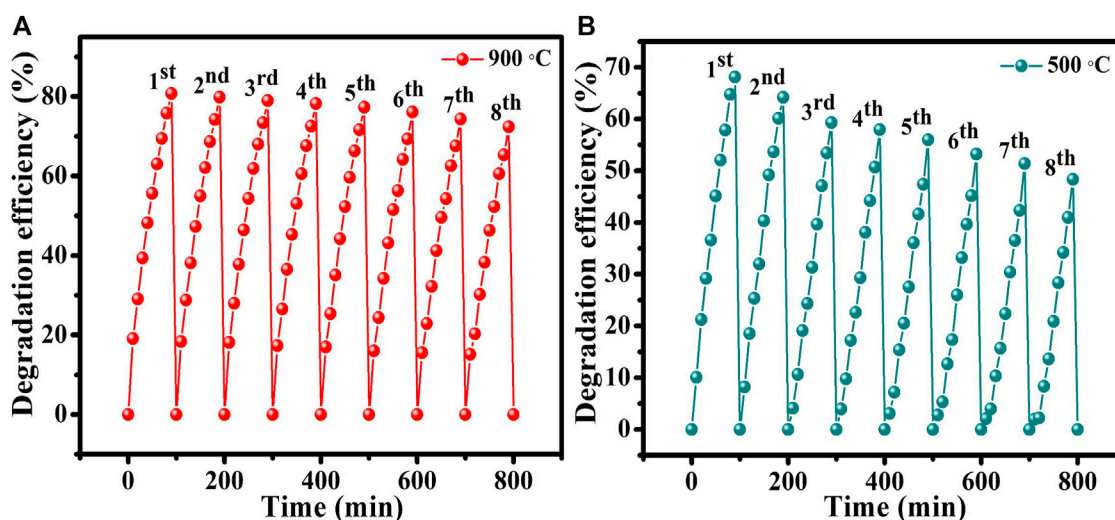
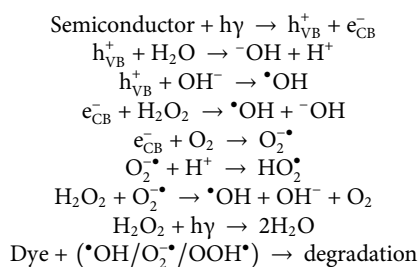


FIGURE 9 Recycling experiment of samples annealed at (A) 900°C and (B) 500°C.

calculated to be 0.01751 min^{-1} , 0.01333 min^{-1} , and 0.01107 min^{-1} , respectively.

To enhance the photocatalytic activity of the prepared CuTa_2O_6 , H_2O_2 (0.6 mL) was added as a green additive. Figure 8C shows the degradation efficiency of the samples with the addition of H_2O_2 ; they have higher degradation efficiencies than those achieved without H_2O_2 . Therefore, the addition of H_2O_2 substantially enhanced photocatalytic activity. Then, Figure 8D displays the linear increase in the degradation rate. The degradation efficiencies of the samples that were annealed at 500°C, 700°C, and 900°C with added H_2O_2 are calculated to be 82.5%, 87.3%, and 94.7% with estimated rates constants of 0.01251 min^{-1} , 0.01129 min^{-1} and 0.00866 min^{-1} , respectively. Hence, the addition of H_2O_2 achieves the efficient photodegradation of MO in the presence of copper tantalum oxide.

The high-performance activity as a result of adding H_2O_2 can be explained as follows. H_2O_2 acts as a good electron acceptor, accelerating the reaction by increasing the formation of oxidizing radicals, which rapidly degrade the dye molecules. When the photons are incident upon the semiconductor, the photogenerated holes react with H_2O or OH^- and produce hydroxyl radicals ($\cdot\text{OH}$) while the superoxide ($\text{O}_2^{\cdot-}$) and ($\cdot\text{OH}$) radicals are generated by the electrons in the conduction band (e_{CB}^-). The produced $\text{O}_2^{\cdot-}$ radicals further form hydroperoxy (OOH^{\cdot}) and $\cdot\text{OH}$ radicals, which destroy the organic contaminants. The possible chemical reactions for the degradation of organic dyes are as follows.



To investigate the stability and reusability of the catalysts, an experiment on the recycling of the samples that were annealed at 500°C and 900°C was conducted. The catalyst sample annealed at 900°C underwent little change or deactivation, as shown in Figure 9A. The sample annealed at 500°C exhibits a considerable decrease in the efficiency of photodegradation, as shown in Figure 9B. Notably, the photodegradation efficiency experiences a rapid decline as early as the second and third runs. Therefore, it is believed that the cubic phase of CuTa_2O_6 is more stable for the photodegradation of MO dye than the orthorhombic phase (sample that was annealed at 500°C).

4 Conclusion

This work demonstrates the photocatalytic activity of the CuTa_2O_6 phase prepared at different annealing temperatures. The structure, morphology, optical properties, and elemental composition were studied using XRD, FESEM, UV-Vis DRS, and XPS. Structural studies confirmed the phase change from orthorhombic to cubic as the temperature of annealing increased. Both phases had the same morphology and exhibited significant visible light absorption. The cubic phase of CuTa_2O_6 supported a higher MO dye degradation efficiency than the orthorhombic phase. The local atomic and electronic structures around Cu and the oxidation state of Cu in the CuTa_2O_6 system were determined by X-ray absorption spectroscopy. The effect of the addition of H_2O_2 to the prepared samples was determined. The above results demonstrate that CuTa_2O_6 can be used as photocatalysts for environmental remediation. The prepared CuTa_2O_6 phase exhibits significant photocatalytic activity and could be a promising photocatalyst in water-splitting applications.

Data availability statement

The original contributions presented in the study are included in the article/[Supplementary Material](#), further inquiries can be directed to the corresponding authors.

Author contributions

Conceptualization: AK and SM Data curation: AK, PM, TT, H-WC, and YM Formal analysis: AK, PM, SM, TT, H-WC, and YM Investigation: AK and SM; Methodology: AK and SM; Supervision: SM; Visualization: SM and C-LD; Writing—original draft: AK, SM, and PM; Writing—review and editing: SM and C-LD. All authors contributed to the article and approved the submitted version.

Acknowledgments

The authors would like to thank the National Science and Technology Council, Taiwan, for financially supporting this research under contracts MOST 110-2112-M-032-013-MY3. The authors are grateful to the support from the beamline staff at BL17C at Taiwan Light Source.

References

- Abdelrahman, E. A., Hegazy, R., Kotp, Y. H., and Alharbi, A. (2019). Facile synthesis of Fe₂O₃ nanoparticles from Egyptian insecticide cans for efficient photocatalytic degradation of methylene blue and crystal violet dyes. *Spectrochimica Acta Part A Mol. Biomol. Spectrosc.* 222, 117195. doi:10.1016/j.saa.2019.117195
- Ajmal, A., Majeed, I., Malik, N., Idriss, H., and Nadeem, M. A. (2014). Principles and mechanisms of photocatalytic dye degradation on TiO₂ based photocatalysts: A comparative overview. *RSC Adv.* 4, 37003–37026. doi:10.1039/c4ra06658h
- Bera, P., Priolkar, K., Sarode, P., Hegde, M., Emura, S., Kumashiro, R., et al. (2002). Structural investigation of combustion synthesized Cu/CeO₂ catalysts by EXAFS and other physical techniques: Formation of a Ce_{1-x}Cu_xO_{2-δ} solid solution. *Chem. Mater.* 14, 3591–3601. doi:10.1021/cm0201706
- Chennakesavulu, K., and Ramajanya Reddy, G. (2015). Synthesis and characterization of carbon microtube/tantalum oxide composites and their photocatalytic activity under visible irradiation. *RSC Adv.* 5, 56391–56400. doi:10.1039/c5ra06812f
- Djurišić, A. B., Leung, Y. H., and Ching Ng, A. M. (2014). Strategies for improving the efficiency of semiconductor metal oxide photocatalysis. *Mater. Horizons.* 1, 400. doi:10.1039/c4mh00031e
- Dutta, D. P., Ballal, A., Fulekar, M. K., and Tyagi, A. K. (2013). Multifunctionality of rare Earth doped nano ZnSb₂O₆, CdSb₂O₆ and BaSb₂O₆: Photocatalytic properties and white light emission. *Dalton Trans.* 42, 16887–16897. doi:10.1039/c3dt51966j
- Gheytanzadeh, M., Baghban, A., Habibzadeh, S., Jabbour, K., Esmaili, A., Mohaddespour, A., et al. (2022). An insight into tetracycline photocatalytic degradation by MOFs using the artificial intelligence technique. *Sci. Rep.* 12, 6615–6711. doi:10.1038/s41598-022-10563-8
- Golubev, A., Dinnebier, R. E., Schulz, A., Kremer, R. K., Langbein, H., Senyshyn, A., et al. (2017). Structural and magnetic properties of the trirutile-type 1D-Heisenberg anti-ferromagnet CuTa₂O₆. *Inorg. Chem.* 56, 6318–6329. doi:10.1021/acs.inorgchem.7b00421
- Gomes, L. E., da Silva, M. F., Goncalves, R. V., Machado, G., Alcantara, G. B., Caires, A. R., et al. (2018). Synthesis and visible-light-driven photocatalytic activity of Ta⁴⁺ self-doped gray Ta₂O₅ nanoparticles. *J. Phys. Chem. C* 122 (11), 6014–6025. doi:10.1021/acs.jpcc.7b11822
- Hodges, B. C., Cates, E. L., and Kim, J. (2018). Challenges and prospects of advanced oxidation water treatment processes using catalytic nanomaterials. *Nat. Nanotechnol.* 13, 642–650. doi:10.1038/s41565-018-0216-x
- Kato, M., Ishii, T., Kajimoto, K., Yoshimura, K., Kosuge, K., Nishi, M., et al. (2002). Magnetic properties of CuSb_{2-x}Ta_xO₆ with tri-rutile structure. *J. Phys. Chem. Solid.* 63, 1129–1132. doi:10.1016/s0022-3697(02)00026-4
- Kau, L. S., Spira-Solomon, D. J., Penner-Hahn, J. E., Hodgson, K. O., and Solomon, E. I. (1987). X-ray absorption edge determination of the oxidation state and coordination

Conflict of interest

The authors declare that the research was conducted in the absence of any commercial or financial relationships that could be construed as a potential conflict of interest.

Publisher's note

All claims expressed in this article are solely those of the authors and do not necessarily represent those of their affiliated organizations, or those of the publisher, the editors and the reviewers. Any product that may be evaluated in this article, or claim that may be made by its manufacturer, is not guaranteed or endorsed by the publisher.

Supplementary material

The Supplementary Material for this article can be found online at: <https://www.frontiersin.org/articles/10.3389/fchem.2023.1197961/full#supplementary-material>

number of copper. Application to the type 3 site in Rhus vernicifera laccase and its reaction with oxygen. *J. Am. Chem. Soc.* 109, 6433–6442. doi:10.1021/ja00255a032

Khalid, N. R., Ahmed, E., Hong, Z., Ahmad, M., Zhang, Y., and Khalid, S. (2013). Cuproed TiO₂ nanoparticles/graphene composites for efficient visible-light photocatalysis. *Ceram. Int.* 39, 7107–7113. doi:10.1016/j.ceramint.2013.02.051

Khemthong, P., Photai, P., and Grisdanurak, N. (2013). Structural properties of CuO/TiO₂ nanorod in relation to their catalytic activity for simultaneous hydrogen production under solar light. *Int. J. hydrogen energy* 38, 15992–16001. doi:10.1016/j.ijhydene.2013.10.065

Krabbes, I., and Langbein, H. (1996). Herstellung von CuTa₂O₆ von der Trirutil-zur Perowskit-Struktur. *Zeit. Naturf.* 51, 1605–1610. doi:10.1515/znbn-1996-1113

Li, J., Sun, F., Gu, K., Wu, T., Zhai, W., Li, W., et al. (2011). Applied Catalysis A: General Preparation of spindle CuO micro-particles for photodegradation of dye pollutants under a halogen tungsten lamp. *Appl. Catal. A, Gen.* 406, 51–58. doi:10.1016/j.apcata.2011.08.007

Li, M., Zhang, H., Zhao, Z., Wang, P., Li, Y., and Zhan, S. (2023). Inorganic ultrathin 2D photocatalysts: Modulation strategies and environmental/energy applications. *Acc. Mater. Res.* 4 (1), 4–15. doi:10.1021/accountsmr.2c00172

Liang, P., Zhang, C., Sun, H., Liu, S., Tade, M., and Wang, S. (2017). Solar photocatalytic water oxidation and purification on ZIF-8-derived C–N–ZnO composites. *Energy & Fuels* 31, 2138–2143. doi:10.1021/acs.energyfuels.6b02057

Lim, H., Thomas, K. E., Hedman, B., Hodgson, K. O., Ghosh, A., and Solomon, E. I. (2019). X-Ray absorption spectroscopy as a probe of ligand noninnocence in metalocorroles: The case of copper corroles. *Inorg. Chem.* 58, 6722–6730. doi:10.1021/acs.inorgchem.9b00128

Liu, H., Gou, X., Wang, Y., Du, X., Quan, C., and Qi, T. (2015). Cauliflower-like Co₃O₄/three-dimensional graphene composite for high performance supercapacitor applications. *J. Nanomater.* 2015, 1–9. doi:10.1155/2015/874245

Louis, J., Padmanabhan, N. T., Jayaraj, M. K., and John, H. (2022). Crystal lattice engineering in a screw-dislocated ZnO nanocone photocatalyst by carbon doping. *Mater. Adv.* 3 (3), 4322–4333. doi:10.1039/d2ma00098a

Mageshwari, K., Sathyamoorthy, R., and Patil, P. S. (2013). Template-free synthesis of MgO nanoparticles for effective photocatalytic applications. *Powder Technol.* 249, 456–462. doi:10.1016/j.powtec.2013.09.016

Majhi, D., Mishra, A. K., Das, K., Bariki, R., and Mishra, B. G. (2021). Plasmonic Ag nanoparticle decorated Bi₂O₃/CuBi₂O₄ photocatalyst for expeditious degradation of 17 α -ethinylestradiol and Cr(VI) reduction: Insight into electron transfer mechanism and enhanced photocatalytic activity. *Chem. Eng. J.* 413, 127506. doi:10.1016/j.cej.2020.127506

Muthu Gnana Theresa Nathana, D., Jacob Melvin Boby, S., Basu, P., Mahesh, R., Harish, S., Joseph, S., et al. (2018). One-pot hydrothermal preparation of Cu₂O-CuO/

rGO nanocomposites with enhanced electrochemical performance for supercapacitor applications. *Appl. Surf. Sci.* 449, 474–484. doi:10.1016/j.apsusc.2017.12.199

Nasir, M., Patra, N., Ahmed, M. A., Shukla, D. K., Kumar, S., Bhattacharya, D., et al. (2017). Role of compensating Li/Fe incorporation in $\text{Cu}_{0.945}\text{Fe}_{0.055}\text{Li}_2\text{O}$: Structural, vibrational and magnetic properties. *RSC Adv.* 7, 31970–31979. doi:10.1039/c7ra03960c

Nguyen, H., Petitbon, F., and Fabry, P. (1996). Investigations on the mixed conductivity of copper tantalate. *Solid State Ionics* 92, 183–192. doi:10.1016/s0167-2738(96)00492-4

Noto, L. L., Chitambo, M. L., Ntwaeaborwa, O. M., and Swart, H. C. (2013). Photoluminescence and thermoluminescence properties of Pr^{3+} doped ZnTa_2O_6 phosphor. *Powder Technol.* 247, 147–150. doi:10.1016/j.powtec.2013.07.012

Oyewo, O. A., Ramaila, S., Mavuru, L., and Onwudiwe, D. C. (2022). Enhanced photocatalytic degradation of methyl orange using Sn-ZnO/GO nanocomposite. *J. Photochem. Photobiol.* 11, 100131. doi:10.1016/j.jpap.2022.100131

Ramchiary, A. (2020). “Metal-oxide semiconductor photocatalysts for the degradation of organic contaminants,” in *Handbook of smart photocatalytic materials* (Elsevier), 23–38.

Rose, A., Hofmann, A., Voepel, P., Milow, B., and Marschall, R. (2022). Photocatalytic activity and electron storage capability of TiO_2 aerogels with an adjustable surface area. *ACS Appl. Energy Mater.* 5, 14966–14978. doi:10.1021/acsaem.2c02517

Sahoo, D., Shakya, J., Ali, N., Yoo, W. J., and Kaviraj, B. (2022). Edge rich ultrathin layered MoS_2 nanostructures for superior visible light photocatalytic activity. *Langmuir* 38 (4), 1578–1588. doi:10.1021/acs.langmuir.1c03013

Sibhatu, A. K., Weldegebriela, G. K., Sagadevan, S., Tran, N. N., and Hessel, V. (2022). Photocatalytic activity of CuO nanoparticles for organic and inorganic pollutants removal in wastewater remediation. *Chemosphere* 300, 134623. doi:10.1016/j.chemosphere.2022.134623

Sullivan, I., Zoellner, B., and Maggard, P. A. (2016). Copper(I)-Based p-type oxides for photoelectrochemical and photovoltaic solar energy conversion. *Chem. Mater.* 28 (17), 5999–6016. doi:10.1021/acs.chemmater.6b00926

Suzuki, T. M., Saeki, S., Sekizawa, K., Kitazumi, K., Takahashi, N., and Morikawa, T. (2017). Photoelectrochemical hydrogen production by water splitting over dual-functionally modified oxide: p-Type N-doped Ta_2O_5 photocathode active under visible light irradiation. *Appl. Catal. B Environ.* 202, 597–604. doi:10.1016/j.apcatb.2016.09.066

Swintsitskiy, D. A., Chupakhin, A. P., Slavinskaya, E. M., Stonkus, O. A., Stadnichenko, A. I., Koscheev, S. V., et al. (2013). Study of cupric oxide nanopowders as efficient catalysts for low-temperature CO oxidation. *J. Mol. Catal. A Chem.* 368, 95–106. doi:10.1016/j.molcata.2012.11.015

Tao, C., Xu, L., and Guan, J. (2013). Well-dispersed mesoporous Ta_2O_5 submicrospheres: Enhanced photocatalytic activity by tuning heating rate at calcination. *Chem. Eng. J.* 229, 371–377. doi:10.1016/j.cej.2013.06.012

Vincent, H., Bochu, B., Aubert, J. J., Joubert, J. C., and Marezio, M. (1978). Structure cristalline de CuTa_2O_6 . *J. Solid State Chem.* 24, 245–253. doi:10.1016/0022-4596(78)90016-6

Wang, Z., Wang, J., Hou, J., Huang, K., Jiao, S., and Zhu, H. (2012). Facile synthesis of efficient photocatalytic tantalum nitride nanoparticles. *Mater. Res. Bull.* 47, 3605–3611. doi:10.1016/j.materresbull.2012.06.054

Xia, H., Wang, Y., Lin, J., and Lu, L. (2012). Hydrothermal synthesis of MnO_2/CNT nanocomposite with a CNT core/porous MnO_2 sheath hierarchy architecture for supercapacitors. *Nanoscale Res. Lett.* 7, 33. doi:10.1186/1556-276x-7-33

Xu, L., Li, C., Shi, W., Guan, J., and Sun, Z. (2012b). Visible light-response $\text{NaTa}_{1-x}\text{Cu}_x\text{O}_3$ photocatalysts for hydrogen production from methanol aqueous solution. *J. Mol. Catal. A, Chem.* 360, 42–47. doi:10.1016/j.molcata.2012.04.006

Xu, L., Steinmiller, E. M., and Skrabalak, S. E. (2012a). Achieving synergy with a potential photocatalytic Z-scheme: Synthesis and evaluation of nitrogen-doped $\text{TiO}_2/\text{SnO}_2$ composites. *J. Phys. Chem. C* 116, 871–877. doi:10.1021/jp208981h

Yang, X., Zhang, S., Li, P., Gao, S., and Cao, R. (2020). Visible-light-driven photocatalytic selective organic oxidation reactions. *Mater. Chem. A* 8, 20897–20924. doi:10.1039/d0ta05485b

Zhang, L. S., Wang, W. Z., Yang, J., Chen, Z. G., Zhang, W. Q., Zhou, L., et al. (2006). Sonochemical synthesis of nanocrystallite Bi_2O_3 as a visible-light-driven photocatalyst. *Appl. Catal. A Gen.* 308, 105–110. doi:10.1016/j.apcata.2006.04.016

Zhang, P., Zhang, J., and Gong, J. (2014). Tantalum-based semiconductors for solar water splitting. *Chem. Soc. Rev.* 43, 4395–4422. doi:10.1039/C3CS60438A

Zhou, L., Wang, W. Z., Xu, H. L., Sun, S. M., and Shang, M. (2009). Bi_2O_3 hierarchical nanostructures: Controllable synthesis, growth mechanism, and their application in photocatalysis. *Chem. Eur. J.* 15, 1776–1782. doi:10.1002/chem.200801234